

# Inferring dark matter substructure with astrometric lensing beyond the power spectrum

ANONYMOUS AUTHOR(S)

## ABSTRACT

Astrometry—the precise measurement of positions and motions of celestial objects—has emerged as a promising avenue for characterizing the dark matter population in our Galaxy. By leveraging recent advances in simulation-based inference and neural network architectures, we introduce a novel method to search for global dark matter-induced gravitational lensing signatures in astrometric datasets. Our method based on neural likelihood-ratio estimation shows significantly enhanced sensitivity to a cold dark matter population and more favorable scaling with measurement noise compared to existing approaches based on two-point correlation statistics, establishing machine learning as a powerful tool for characterizing dark matter using astrometric data.

*Keywords:* astrostatistics techniques (1886) — cosmology (343) — dark matter (353) — gravitational lensing (670) — convolutional neural networks (1938) — astrometry (80)

## 1. INTRODUCTION AND BACKGROUND

Although there exists plenty of evidence for dark matter (DM) on galactic scales and above (see [Green \(2021\)](#) for a recent overview), the distribution of DM clumps—subhalos—on sub-galactic scales is less well-understood and remains an active area of cosmological study. This distribution additionally correlates with and may provide clues about the underlying particle physics nature of dark matter (see e.g., [Schutz \(2020\)](#); [Bode et al. \(2001\)](#); [Dalcanton & Hogan \(2001\)](#)), highlighting its relevance across multiple domains.

While more massive dark matter subhalos can be detected and studied through their association with luminous tracers such as bound stellar populations, subhalos with smaller masses  $\lesssim 10^9 M_\odot$  are not generally associated with luminous matter ([Fitts et al. 2017](#); [Read et al. 2017](#)), rendering their characterization challenging. Gravitational effects provide one of the few avenues to probe the distribution of these otherwise-invisible subhalos ([Buckley & Peter 2018](#)). Gravitational lensing i.e., the bending of light from a background source due to a foreground mass, is one such effect and has been proposed in various incarnations as a probe of dark subhalos. Strong gravitational lensing, for example, has been used to infer the presence of dark matter substructure in galaxies outside of our own ([Hezaveh et al. 2016](#); [Vegetti et al. 2010](#); [Gilman et al. 2020](#); [Vegetti et al. 2012](#)). Astrometric lensing, on the other hand, has recently emerged as a promising way to characterize the dark matter subhalo population within the Milky Way.

Astrometry refers to the precise measurement of the positions and motions of luminous celestial objects like stars and galaxies. Gravitational lensing of these background objects by a moving foreground mass, such as a dark matter subhalo, can imprint a characteristic, correlated signal on their measured kinematics (angular velocities and/or accelerations). [Van Tilburg et al. \(2018\)](#) introduced several methods for extracting this signature, including computing convolutions of the expected lensing signal on astrometric datasets and detecting local kinematic outliers. [Mondino et al. \(2020\)](#) applied the former method to data from the *Gaia* satellite, obtaining constraints on the abundance of dark compact objects in the Milky Way and showcasing the applicability of astrometric dark matter searches in a practical setting. Finally, [Mishra-Sharma et al. \(2020\)](#) proposed using the angular power spectrum of the astrometric field as an observable to infer the population properties of subhalos in our Galaxy, leveraging the collective, correlated signal of a large subhalo sample.

Astrometric datasets are inherently high-dimensional, consisting of positions and kinematics of potentially millions of objects. Especially when the expected signal consists of the collective imprint of a large number of lenses, characterizing their population properties involves marginalizing over all possible configurations of subhalos, rendering the likelihood intractable and usually necessitating the use of simplified data representations like the power spectrum. While effective, such simplification can result in loss of information compared to that contained in the original dataset when the ex-

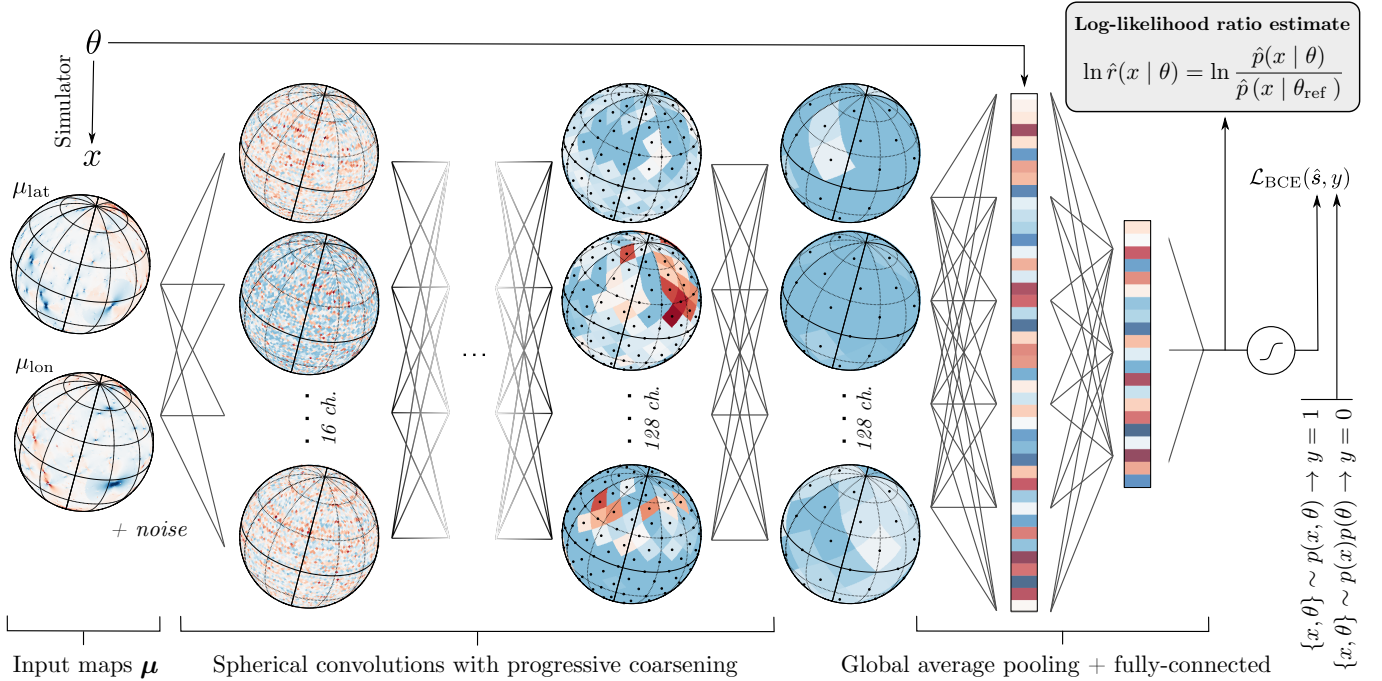


**Figure 1.** A schematic illustration of the method and neural network architecture used in this work.

pected signal is non-Gaussian in nature. The existence of systematic effects that are degenerate with a putative signal in the low-dimensional summary domain can further inhibit sensitivity.

The dawn of the era of precision astrometry, with the *Gaia* satellite (Gaia Collaboration 2016) having recently delivered the most precise astrometric dataset to-date (Gaia Collaboration 2018a; Lindegren et al. 2018; Gaia Collaboration 2021) and surveys including the Square Kilometer Array (SKA) (Fomalont & Reid 2004; Jarvis et al. 2015) and Roman Space Telescope (WFIRST Astrometry Working Group 2019) set to achieve further leaps in sensitivity over the next decade, calls for methods that can extract more information from these datasets than is possible using existing techniques. In this direction, Vattis et al. (2020) proposed using a binary classifier in order to detect either the presence or absence of a substructure signal in astrometric maps. In this paper, we introduce an *inference* approach that uses spherical convolutional neural networks—exploiting the symmetry structure of the signal and data domain—in conjunction with parameterized classifiers (Cranmer et al. 2015; Baldi et al. 2016) in order to estimate likelihood ratios associated with the abundance of a cold dark matter population directly from a binned map of the astrometric velocity field. We show that our method outperforms established proposals based on the two-point correlation statistics of the

astrometric field, both in absolute sensitivity as well as its scaling with measurement noise.

## 2. MODEL AND INFERENCE

### 2.1. The forward model

We consider a population of Navarro-Frenk-White (NFW) (Navarro et al. 1996) subhalos following a power-law mass function,  $dn/dm \propto m^\alpha$ , with slope  $\alpha = -1.9$  as expected if the population is sourced from nearly scale-invariant primordial fluctuations in the canonical  $\Lambda$  Cold Dark Matter ( $\Lambda$ CDM) scenario. The concentration-mass relation from Sánchez-Conde & Prada (2014) is used to model the concentrations associated with density profiles of individual subhalos.

Subhalos between  $10^7$ – $10^{10} M_\odot$  are simulated, assuming the influence of lighter subhalos to be too small to be discernable (Mishra-Sharma et al. 2020). The subhalo fraction  $f_{\text{sub}}$ , quantifying the expected fraction of the mass of the Milky Way contributed by subhalos in the range  $10^{-6}$ – $10^{10} M_\odot$ , is taken to be the parameter of interest. The spatial distribution of subhalos in the Galactocentric frame is modeled using results from the Aquarius simulation following Hütten et al. (2016); Springel et al. (2008). Since this spatial distribution accounts for the depletion of subhalos towards the Galactic Center due to gravitational tidal effects, the angular number density of subhalos looking out from the Sun frame can be considered to be effectively isotropic.

The asymptotic velocities of subhalos in the Galactocentric frame are taken to follow a truncated Maxwell-Boltzmann distribution (Chandrasekhar 1939; Lisanti 2017)  $f_{\text{Gal}}(\mathbf{v}) \propto e^{-\mathbf{v}^2/v_0^2} \cdot H(v_{\text{esc}} - |\mathbf{v}|)$ , where  $v_{\text{esc}} = 550 \text{ km s}^{-1}$  is the Galactic escape velocity (Piffi et al. 2014),  $v_0 = 220 \text{ km s}^{-1}$  (Kerr & Lynden-Bell 1986), and  $H$  is the Heaviside step function. Once instantiated, the positions and velocities of subhalos are transformed into the Galactic frame, assuming  $R_{\odot} = 8.2 \text{ kpc}$  to be the distance of the Sun from the Galactic Center (Gravity Collaboration 2019; Bovy 2020) and  $\mathbf{v}_{\odot} = (11, 232, 7) \text{ km s}^{-1}$  its Galactocentric velocity (Schönrich et al. 2010). Note that the asymmetry in the direction of motion of the Sun in the Milky Way introduces a preferred direction for the Sun-frame velocities of subhalos, breaking strict rotation invariance in the forward model. Although not explicitly pursued here, this asymmetry can be used as an additional distinguishing handle for the lensing signal, as was done in Mishra-Sharma et al. (2020).

Our datasets consist of the 2-dimensional angular velocity map of background sources on the celestial sphere. Given a spherically-symmetric subhalo lens moving with transverse velocity  $\mathbf{v}_l$ , the expected lens-induced velocity for a quasar at impact parameter  $\mathbf{b}$  is given by (Van Tilburg et al. 2018)

$$\boldsymbol{\mu}(\mathbf{b}) = 4G_N \left\{ \frac{M(b)}{b^2} [2\hat{\mathbf{b}}(\hat{\mathbf{b}} \cdot \mathbf{v}_l) - \mathbf{v}_l] - \frac{M'(b)}{b} \hat{\mathbf{b}}(\hat{\mathbf{b}} \cdot \mathbf{v}_l) \right\} \quad (1)$$

where  $M(b)$  and  $M'(b)$  are the projected mass of the subhalo at a given impact parameter distance  $b = |\mathbf{b}|$  and its gradient. An example of the induced velocity signal on part of the celestial sphere, projected along the Galactic latitudinal and longitudinal directions and exhibiting dipole-like structures, is shown in the leftmost column of Fig. 1.

We take our source population to consist of remote, point-like galaxies known as quasars which, due to their large distances from the Earth, are not expected to have significant intrinsic angular velocities. We assume the sources to be isotropically-distributed, although this assumption can be easily relaxed for a realistic source sample. The velocity maps are assumed to be spatially binned, and we use a *HEALPix* binning (Gorski et al. 2005) with resolution parameter `nside=64`, corresponding to  $N_{\text{pix}} = 49,152$  pixels over the full sky with pixel area  $\sim 0.8 \text{ deg}^2$ . The values within each pixel then quantify the average latitudinal and longitudinal velocity components of quasars within that pixel, with the impact parameter  $\mathbf{b}$  representing the vector from the center of a subhalo to the center of the pixel.

In order to enable a comparison with traditional approaches—which are generally not expected to be sen-

sitive to a cold dark matter subhalo population with next-generation astrometric surveys (Van Tilburg et al. 2018; Mishra-Sharma et al. 2020)—we benchmark using an optimistic observational configuration corresponding to measuring the proper motions of  $N_q = 10^8$  quasars with noise  $\sigma_{\mu} = 0.1 \mu\text{as yr}^{-1}$ .

## 2.2. The power spectrum approach

Mishra-Sharma et al. (2020) introduced an approach for extracting the astrometric signal due to a dark matter subhalo population by decomposing the observed map into its angular (vector) power spectrum. The power spectrum is a summary statistic ubiquitous in astrophysics and cosmology and quantifies the amount of correlation contained at different spatial scales. In the case of data on a sphere, the basis of spherical harmonics is often used, and the power spectrum then encodes the correlation structure on different multipoles  $\ell$ . The power spectrum effectively captures the linear component of the signal and, when the underlying signal is a Gaussian random field, captures *all* of the relevant information contained in the map(s) (Tegmark 1997). The expected signal in the power spectrum domain can be evaluated semi-analytically using the formalism described in Mishra-Sharma et al. (2020) and, assuming a Gaussian likelihood, the expected sensitivity can be computed using a Fisher forecasting approach. We use this prescription as a comparison point to the method introduced here.

While effective, reduction of the full astrometric map to its power spectrum results in loss of information; this can be seen from the fact that the signal in the leftmost column of Fig. 1 is far from Gaussian. Furthermore, the existence of correlations on large angular scales due to e.g., biases in calibration of celestial reference frames (Gaia Collaboration 2018b) or systematic variations in measurements taken over different regions of the sky introduces degeneracies with a putative signal and precludes their usage in the present context. For this reason multipoles  $\ell < 10$  were discarded in Mishra-Sharma et al. (2020), degrading the projected sensitivity.

## 2.3. Likelihood-ratio estimation using parameterized classifiers

Recent advances in machine learning have enabled methods that can be used to efficiently perform inference on models defined through complex simulations; see Cranmer et al. (2020) for a recent review. Here, we make use of neural likelihood-ratio estimation (Cranmer et al. 2015; Baldi et al. 2016; Brehmer et al. 2018a, 2020, 2018b; Hermans et al. 2019), previously applied to the problem of inferring dark matter substructure using ob-

servations of strong gravitational lenses (Brehmer et al. 2019) and cold stellar streams (Hermans et al. 2020).

Given a classifier that can distinguish between samples  $\{x\} \sim p(x | \theta)$  drawn from parameter points  $\theta$  and those from a fixed reference hypothesis  $\{x\} \sim p(x | \theta_{\text{ref}})$ , the decision function output by the optimal classifier  $s(x, \theta) = p(x | \theta) / (p(x | \theta) + p(x | \theta_{\text{ref}}))$  is one-to-one with the likelihood ratio,  $r(x | \theta) \equiv p(x | \theta) / p(x | \theta_{\text{ref}}) = s(x, \theta) / (1 - s(x, \theta))$ , a fact appreciated as the likelihood-ratio trick (Cranmer et al. 2015; Mohamed & Lakshminarayanan 2017). The classifier  $s(x, \theta)$  in this case is a neural network that can work directly on the high-dimensional data  $x$ , and is parameterized by  $\theta$  by having it included as an input feature. In order to improve numerical stability and reduce dependence on the fixed reference hypothesis  $\theta_{\text{ref}}$ , we follow Hermans et al. (2019) and train a classifier to distinguish between data-sample pairs from the joint distribution  $\{x, \theta\} \sim p(x, \theta)$  and those from a product of marginal distributions  $\{x, \theta\} \sim p(x)p(\theta)$  (defining the reference hypothesis and in practice obtained by shuffling samples within a batch) using the binary cross-entropy (BCE) loss as the optimization objective.

#### 2.4. Extracting information from high-dimensional astrometric maps

Since our dataset consists of a velocity field sampled on a sphere, we use a spherical convolutional neural network in order to directly learn useful representations from these maps that are efficiently suited for the downstream classification task. Specifically, we make use of *DeepSphere* (Defferrard et al. 2020; Perraudin et al. 2019), a graph-based convolutional neural network tailored to data sampled on a sphere. For this purpose, the *HEALPix* grid can be cast as a weighted undirected graph with  $N_{\text{pix}}$  vertices and edges connecting each pixel vertex to its set of 8 neighboring pixels. The weighted adjacency matrix over neighboring pixels  $(i, j)$  is given by  $A_{ij} = \exp(-\Delta r_{ij}^2 / \rho^2)$  where  $\Delta r_{ij}$  specifies the 3-dimensional Euclidean distance between the pixel centers and the widths  $\rho$  are obtained from Defferrard et al. (2020). *DeepSphere* then efficiently performs convolutions in the spectral domain using a basis of Chebychev polynomials as convolutional kernels (Defferrard et al. 2016); here, we set  $K = 4$  as the maximum polynomial order.

All inputs are normalized to zero mean and unit standard deviation across the training sample. Starting with 2 scalar input channels representing the two orthogonal (Galactic latitude and longitude) components of the

velocity vector map,<sup>1</sup> we perform a graph convolution operation, increasing the channel dimension to 16 followed by a batch normalization, ReLU nonlinearity, and downsampling the representation by a factor of 4 with max pooling into the next coarser *HEALPix* resolution. Pooling leverages scale separation, preserving important characteristics of the signal across different resolutions. Four more such layers are employed, increasing the channel dimension by a factor of 2 at each step until a maximum of 128, with maps after the last convolutional layer having resolution `nside=2` corresponding to 48 pixels. At this stage, we average over the spatial dimension (known as global average pooling (Lin et al. 2014)) in order to encourage approximate rotation invariance, outputting 128 features onto which the parameter of interest  $f_{\text{sub}}$  is appended. These features are passed through a fully-connected network with (1024, 128) hidden units and ReLU activations outputting the classifier decision  $\hat{s}$  by applying a sigmoidal projection.

#### 2.5. Model training and evaluation

$10^5$  maps from the forward model were produced, with 15% of these held out for validation. The estimator was trained using a batch size of 64 for up to 50 epochs with early stopping if the validation loss had not improved after 10 epochs. The ADAM optimizer (Kingma & Ba 2017) was used with initial learning rate  $10^{-3}$  decayed through cosine annealing. A coarse grid search was used to inform the architecture and hyperparameter choices in this work.

For a given test map, the log-likelihood ratio profile can be obtained by evaluating the trained estimator for different values of  $f_{\text{sub}}$  while keeping the input map fixed. The network output prior to the final sigmoidal projection directly gives the required log-likelihood ratio estimate:  $\ln \hat{r} = S^{-1}(\hat{s})$ , where  $S$  is the sigmoid function (Hermans et al. 2019, 2020). Figure 1 presents an illustrative summary of the neural network architecture and method used in this work.

### 3. EXPERIMENTS ON SIMULATED DATA

#### 3.1. Baseline results and diagnostics

We evaluate our trained likelihood-ratio estimator on maps drawn from a benchmark configuration moti-

<sup>1</sup> We note that by representing the input angular velocity vector field in terms of two input scalar channels, we break the desired rotation equivariance of spherical convolutions due to differences in how scalar and vector representations transform under rotations. Although this will have a downstream effect on rotation invariance, a detailed study of how this influences the performance of our model is beyond the scope of this paper.



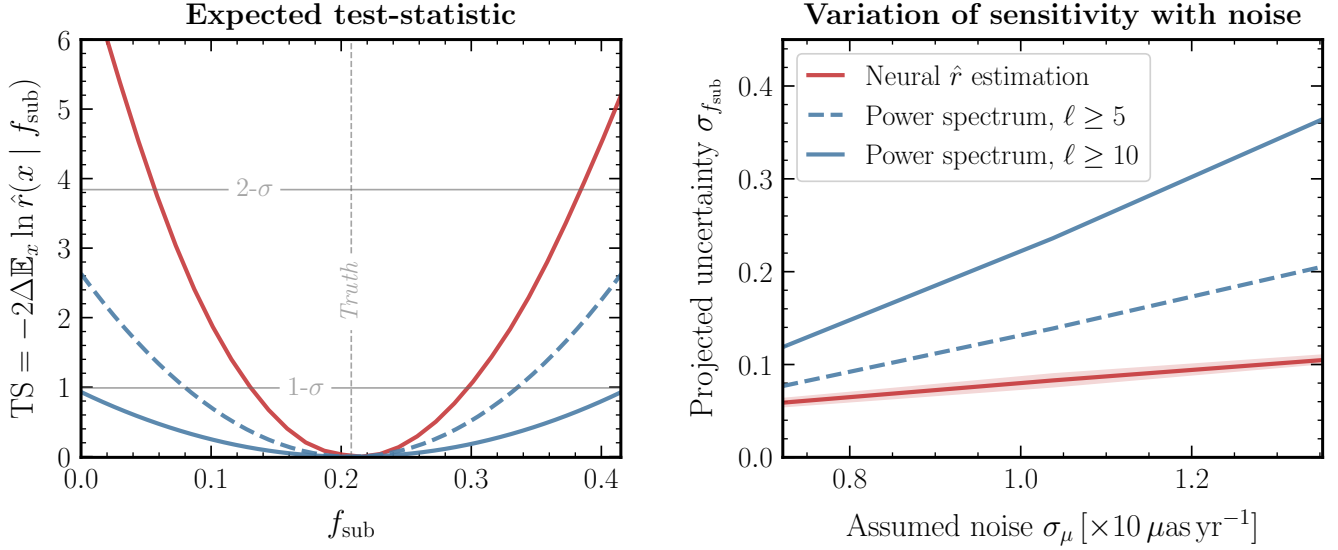


**Figure 2.** (Left) The expected log-likelihood ratio test-statistic (TS) profile for a cold dark matter population as a function of substructure fraction  $f_{\text{sub}}$  obtained using the neural likelihood-ratio estimation method introduced in this work (red line) compared with the corresponding profiles for existing approaches using power spectrum summaries with different multipole thresholds  $\ell \gtrsim 5$  (dashed blue line) and  $\ell \gtrsim 10$  (solid blue line). The vertical dotted line indicates the true benchmark value of the parameter  $f_{\text{sub}}$  in the test dataset. Our method shows enhanced sensitivity to a cold dark matter population compared to traditional approaches. (Right) Scaling of the expected sensitivities, quantified by the respective 1- $\sigma$  uncertainties, with per-object instrumental noise. For the machine learning-based approach, the band quantifies the middle-95% containment of the inferred 1- $\sigma$  uncertainty. Our method shows a more favorable scaling with assumed measurement noise.

vated by Hütten et al. (2016); Springel et al. (2008), containing 150 subhalos in expectation between  $10^8$ – $10^{10} M_{\odot}$  and corresponding to  $f_{\text{sub}} \simeq 0.2$ . The left panel of Fig. 2 shows the expected log-likelihood ratio test-statistic (TS) as a function of substructure fraction  $f_{\text{sub}}$  for this nominal configuration. This is obtained by evaluating the trained estimator on 100 test maps over a uniform grid in  $f_{\text{sub}}$  and taking the point-wise mean. Corresponding curves using the power spectrum approach are shown in blue, using minimum multipoles of  $\ell \geq 5$  (dashed) and  $\ell \geq 10$  (solid). Thresholds corresponding to 1- and 2- $\sigma$  significance assuming a  $\chi^2$ -distributed TS are shown as the horizontal grey lines. We see that sensitivity gains of over a factor of  $\sim 2$  can be expected for this particular benchmark when using the machine learning approach compared to the traditional power spectrum approach. No significant bias on the central value of the inferred DM abundance relative to the overall uncertainty scale is observed.

The right panel of Fig. 2 shows the scaling of expected 1- $\sigma$  uncertainty on substructure fraction  $f_{\text{sub}}$  with assumed noise per quasar, keeping the number of quasars fixed (red, with the line showing the median and shaded band corresponding to the middle-95% containment of the uncertainty inferred over 50 test datasets) compared to the power spectrum approach (blue lines). A far more favorable scaling of the machine learning approach is

seen compared to the power spectrum approach, suggesting that it is especially advantageous in low signal-to-noise regimes that are generally most relevant for dark matter searches.

Finally, we assess the quality of the approximate likelihood-ratio estimator through a test of statistical coverage. Within a hypothesis testing framework, this is necessary in order to ensure that the learned estimator is conservative over the parameter range of interest and does not produced overly confident or biased results (Hermans et al. 2021). We obtain the estimated TS profile for 1000 simulated samples with true substructure fraction values drawn from the range  $f_{\text{sub}} \in [0.1, 0.3]$ . In doing so, we exclude parameter points towards the edges of our parameter space since the corresponding confidence intervals in these cases would extend outside of the tested parameter range, as can also be inferred from the baseline analysis shown in Fig. 2. For nominal confidence levels in the range  $1 - \alpha \in [0.05, 0.95]$  we compute the empirical coverage over the set of samples, defined as the fraction of samples whose true parameter value falls within the TS confidence interval, computed for a given confidence level under the assumption that the TS is  $\chi^2$ -distributed (Wilks 1938). The procedure is repeated for 10 different sets of 1000 samples in order to estimate the statistical uncertainty associated with the empirical coverage.

The results of the coverage test are shown in Fig. 3, illustrating the median (solid red) and middle-68% containment (red band) of the empirical coverage. We see that the empirical coverage has the desired property of being slightly conservative while still being close to the perfectly-calibrated regime indicated by the dashed-grey line. We emphasize that this diagnostic tests the quality of the likelihood-ratio estimator over the entire evaluation parameter range of interest  $f_{\text{sub}} \in [0.1, 0.3]$  rather than the baseline value  $f_{\text{sub}} \simeq 0.2$  in isolation.

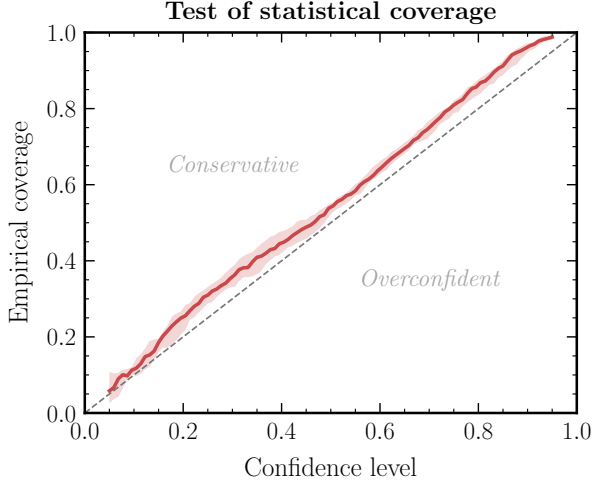


**Figure 3.** Calibration test

### 3.2. Experiments with unmodeled noise correlated on large scales

Since the existence of measurement noise correlated on large spatial scales is a potential source of systematic uncertainty when working with astrometric maps, we test the susceptibility of our method to such effects by creating simulated data containing large-scale noise not previously seen by the trained estimator. Instead of assuming a scale-invariant noise power spectrum  $C_{\ell}^{\text{noise}} = 4\pi\sigma_{\mu}^2/N_q$  (Mishra-Sharma et al. 2020), in this case we model noise with an order of magnitude excess in power on scales  $\ell \lesssim 10$ , parameterized as  $C_{\ell}^{\text{noise}} = 4\pi\sigma_{\mu}^2/N_q \cdot (10 - 9S(\ell - 10))$  where  $S$  denotes the sigmoid function. The left panel of Fig. 4 illustrates this noise model (thicker green line) as well as the power spectrum of one simulated realization from this model (thinner green line, obtained using the *HEALPix* module *anafast*) contrasted with the standard scale-invariant noise case (red lines). The right panel of Fig. 4 shows the expected log-likelihood ratio test-statistic profile for the two cases. Although a bias in the maximum-likelihood estimate of  $f_{\text{sub}}$  is seen when the test data

has unmodeled noise (green line), the true test parameter value (dashed vertical line) is seen to lie well within the inferred  $1\text{-}\sigma$  confidence interval. This suggests that the method is only marginally susceptible to substantive amounts of correlated noise on large spatial scales.

### 3.3. Experiments with a data-driven noise model

We finally assess the performance of our model using a realistic, data-driven noise model obtained using the astrometric catalog of quasars in *Gaia*'s second data release (DR2). The catalog contains the measured 2-dimensional positions, proper motions, as well as proper motion uncertainties of 555,934 quasars. We bin the proper motion uncertainties using the *HEALPix* pixelization used in the analysis, down-weighting the mean variance in each bin by the number of quasars.

## 4. CONCLUSIONS AND OUTLOOK

We have introduced a method to analyze astrometric datasets over large regions of the sky using techniques based on machine learning with the aim of inferring the lensing signature of a dark matter substructure. We have shown our method to be significantly more sensitive to a cold dark matter subhalo population compared to established methods based on global summary statistics, with more favorable scaling as a function of measurement noise. Since the collection and reduction of astrometric data is an expensive endeavor, the use of methods that can take advantage of more of the available information can be equated to long periods of data-taking, underscoring their importance. Additionally, unlike the power spectrum approach, the current method does not require the construction of a numerically-expensive estimator to account for non-uniform exposure, selection effects, and instrumental noise in realistic datasets. These, as well as any other modeled observational effects, can be incorporated directly at the level of the forward model.

We have focused in this work on assessing sensitivity to a cold dark matter-like subhalo population with quasar velocity astrometry, which is within the scope of upcoming radio surveys like the SKA (Fomalont & Reid 2004; Jarvis et al. 2015). Our method can also be applied in a straightforward manner to look for the *acceleration* lensing signal imprinted on Milky Way stars, in particular sourced by a population of more compact subhalos than those expected in the cold dark matter scenario. These features are expected to imprint a larger degree of non-Gaussianity compared to the signal explored here (as can be seen, e.g., from Fig. 1 of Mishra-Sharma et al. (2020)), and machine learning methods may provide larger relative sensitivity gains when deployed in that context. Such analyses are within purview of the

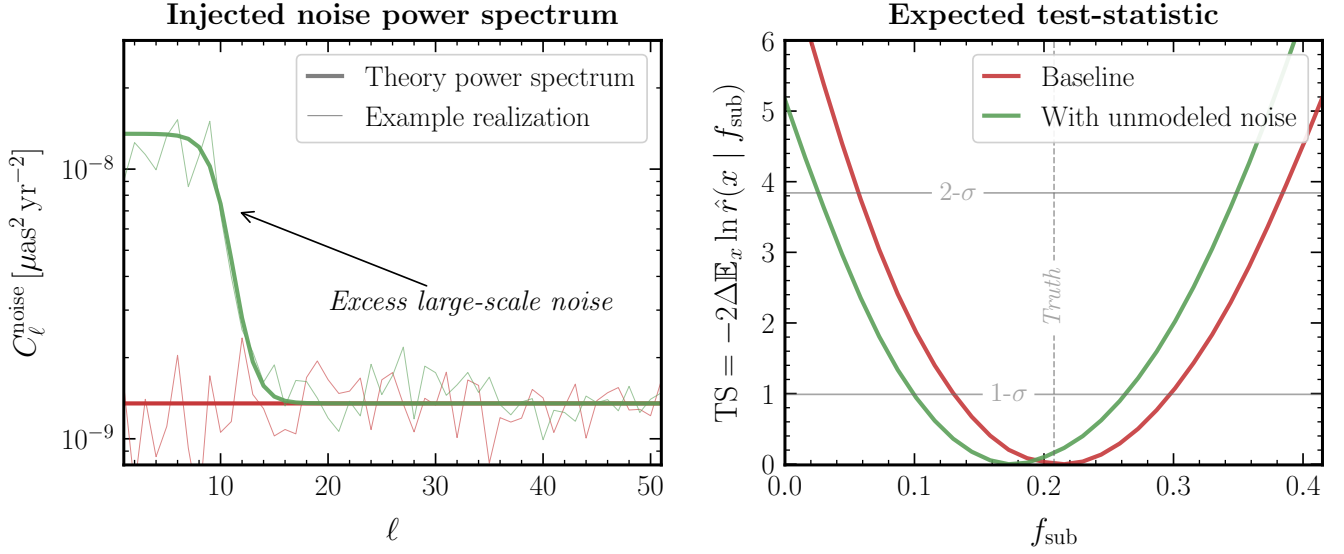


**Figure 4.** (Left) The power spectrum of the noise model (thicker green line) used to study the impact of correlated noise on large spatial scales, not modeled during training, on the performance of the likelihood-ratio estimator. The thinner green line shows the power spectrum of an example noise realization instantiated from this noise model. The red lines show corresponding power spectra for a scale-invariant noise model. (Right) The expected test-statistic profile for a model evaluated on maps containing excess large-scale noise (green line) compared to the model evaluated on maps with scale-invariant noise (red line). A bias in the maximum-likelihood estimate returned by the model is seen when substantial unaccounted-for noise is presented in the test maps.

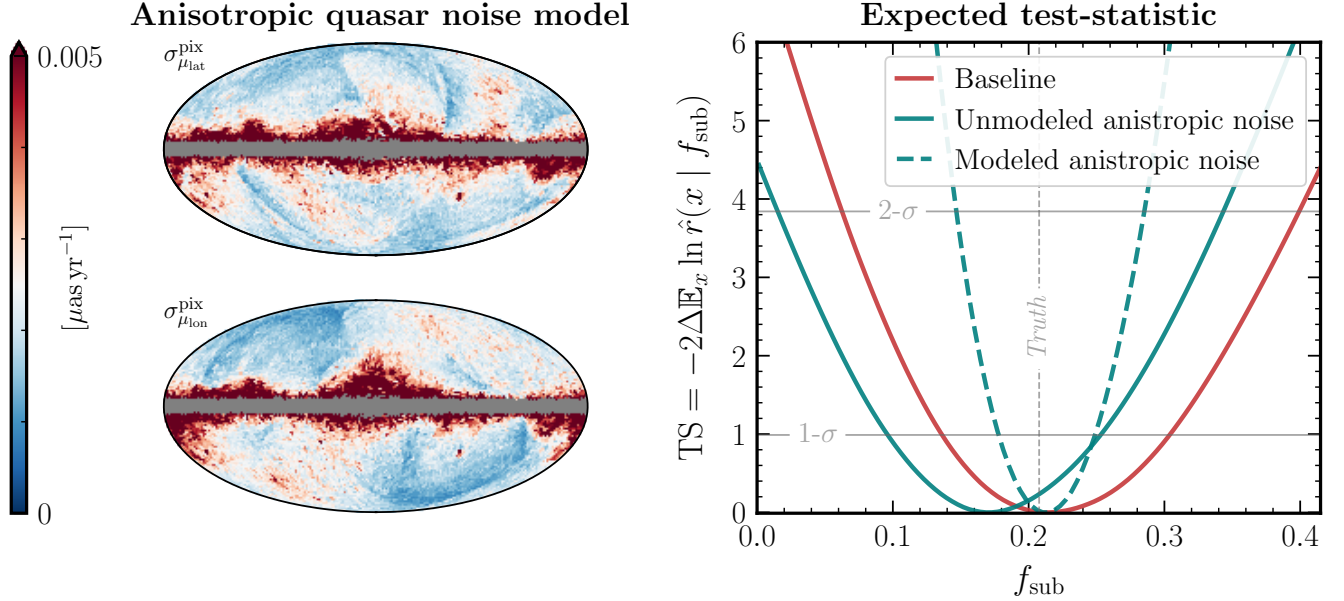


**Figure 5.** (Left) (Right)

upcoming Roman exoplanet microlensing survey (Pardo & Doré 2021) as well as future *Gaia* data releases.

Several improvements and extensions to the method presented in this paper are possible. The use of architectures that can equivariantly handle vector inputs (Esteves et al. 2020) can aid in learning more efficient representations of the astrometric map. Using convolutions based on fixed rather than learned filters can additionally reduce model complexity and produce more interpretable representations (Cheng et al. 2020; Ha et al. 2021; Saydjari & Finkbeiner 2021; McEwen et al. 2021; Valogiannis & Dvorkin 2021). The use of methods for likelihood-ratio estimation that can leverage additional latent information in the forward model can significantly enhance the sample efficiency of the analysis (Brehmer et al. 2018a, 2020, 2018b; Stoye et al. 2018). We leave the study of these extensions as well as application of our method to other dark matter population scenarios to future work.

Astrometric lensing has been established as a promising way to characterize the Galactic dark matter popu-

lation, with theoretical progress in recent years going in step with advances on the observational front. While this work is a first attempt at bringing principled machine learning techniques to this field, with the availability of increasingly complex datasets we expect machine learning to be an important general-purpose tool for future astrometric dark matter searches.

(Acknowledgments anonymized for review)

*Software:* *Astropy* (Robitaille et al. 2013; Price-Whelan et al. 2018), *healpy* (Gorski et al. 2005; Zonca et al. 2019), *IPython* (Pérez & Granger 2007), *Jupyter* (Kluyver et al. 2016), *Matplotlib* (Hunter 2007), *MLflow* (Chen et al. 2020), *NumPy* (Harris et al. 2020), *PyGSP* (Defferrard et al. 2017), *PyTorch* (Paszke et al. 2019), *PyTorch Geometric* (Fey & Lenssen 2019), *PyTorch Lightning* (Falcon et al. 2020), *sbi* (Tejero-Cantero et al. 2020), *SciPy* (Virtanen et al. 2020), and *seaborn* (Waskom et al. 2017).

## REFERENCES

- Baldi, P., Cranmer, K., Faucett, T., Sadowski, P., & Whiteson, D. 2016, *Eur. Phys. J. C*, 76, 235, arXiv: 1601.07913, doi: 10.1140/epjc/s10052-016-4099-4
- Bode, P., Ostriker, J. P., & Turok, N. 2001, *Astrophys. J.*, 556, 93, arXiv: astro-ph/0010389, doi: 10.1086/321541
- Bovy, J. 2020, arXiv: 2012.02169
- Brehmer, J., Cranmer, K., Louppe, G., & Pavez, J. 2018a, *Phys. Rev. D*, 98, 052004, arXiv: 1805.00020, doi: 10.1103/PhysRevD.98.052004
- . 2018b, *Phys. Rev. Lett.*, 121, 111801, arXiv: 1805.00013, doi: 10.1103/PhysRevLett.121.111801
- Brehmer, J., Louppe, G., Pavez, J., & Cranmer, K. 2020, *Proc. Nat. Acad. Sci.*, 117, 5242, arXiv: 1805.12244, doi: 10.1073/pnas.1915980117
- Brehmer, J., Mishra-Sharma, S., Hermans, J., Louppe, G., & Cranmer, K. 2019, *Astrophys. J.*, 886, 49, arXiv: 1909.02005, doi: 10.3847/1538-4357/ab4c41
- Buckley, M. R., & Peter, A. H. G. 2018, *Phys. Rept.*, 761, 1, arXiv: 1712.06615, doi: 10.1016/j.physrep.2018.07.003
- Chandrasekhar, S. 1939, *An introduction to the study of stellar structure*
- Chen, A., et al. 2020, in *Proceedings of the fourth international workshop on data management for end-to-end machine learning*, 1–4
- Cheng, S., Ting, Y.-S., Ménard, B., & Bruna, J. 2020, *Mon. Not. Roy. Astron. Soc.*, 499, 5902, arXiv: 2006.08561, doi: 10.1093/mnras/staa3165
- Cranmer, K., Brehmer, J., & Louppe, G. 2020, *Proc. Nat. Acad. Sci.*, 117, 30055, arXiv: 1911.01429, doi: 10.1073/pnas.1912789117
- Cranmer, K., Pavez, J., & Louppe, G. 2015, arXiv: 1506.02169
- Dalcanton, J. J., & Hogan, C. J. 2001, *Astrophys. J.*, 561, 35, arXiv: astro-ph/0004381, doi: 10.1086/323207
- Defferrard, M., Bresson, X., & Vandergheynst, P. 2016, arXiv: 1606.09375
- Defferrard, M., Martin, L., Pena, R., & Perraudin, N. 2017, *PyGSP: Graph Signal Processing in Python*, v0.5.0, Zenodo, doi: 10.5281/zenodo.1003158, https://doi.org/10.5281/zenodo.1003158
- Defferrard, M., Milani, M., Gusset, F., & Perraudin, N. 2020, arXiv: 2012.15000
- Esteves, C., Makadia, A., & Daniilidis, K. 2020, *Spin-Weighted Spherical CNNs*, arXiv: 2006.10731
- Falcon, W., et al. 2020, *PyTorchLightning/pytorch-lightning: 0.7.6 release*, 0.7.6, Zenodo, doi: 10.5281/zenodo.3828935, https://doi.org/10.5281/zenodo.3828935
- Fey, M., & Lenssen, J. E. 2019, in *ICLR Workshop on Representation Learning on Graphs and Manifolds*
- Fitts, A., et al. 2017, *Mon. Not. Roy. Astron. Soc.*, 471, 3547, arXiv: 1611.02281, doi: 10.1093/mnras/stx1757



- Fomalont, E. B., & Reid, M. 2004, *New Astron. Rev.*, 48, 1473, arXiv: [astro-ph/0409611](#), doi: [10.1016/j.newar.2004.09.037](#)
- Gaia Collaboration. 2016, *Astron. Astrophys.*, 595, A1, arXiv: [1609.04153](#), doi: [10.1051/0004-6361/201629272](#)
- . 2018a, *Astron. Astrophys.*, 616, A1, arXiv: [1804.09365](#), doi: [10.1051/0004-6361/201833051](#)
- . 2018b, *Astron. Astrophys.*, 616, A14, arXiv: [1804.09377](#), doi: [10.1051/0004-6361/201832916](#)
- . 2021, *Astron. Astrophys.*, 649, A1, arXiv: [2012.01533](#), doi: [10.1051/0004-6361/202039657](#)
- Gilman, D., Birrer, S., Nierenberg, A., et al. 2020, *Mon. Not. Roy. Astron. Soc.*, 491, 6077, arXiv: [1908.06983](#), doi: [10.1093/mnras/stz3480](#)
- Gorski, K. M., Hivon, E., Banday, A. J., et al. 2005, *Astrophys. J.*, 622, 759, arXiv: [astro-ph/0409513](#), doi: [10.1086/427976](#)
- Gravity Collaboration. 2019, *Astron. Astrophys.*, 625, L10, arXiv: [1904.05721](#), doi: [10.1051/0004-6361/201935656](#)
- Green, A. M. 2021, in *Les Houches summer school on Dark Matter*
- Ha, W., Singh, C., Lanusse, F., Upadhyayula, S., & Yu, B. 2021, arXiv: [2107.09145](#)
- Harris, C. R., et al. 2020, *Nature*, 585, 357, doi: [10.1038/s41586-020-2649-2](#)
- Hermans, J., Banik, N., Weniger, C., Bertone, G., & Louppe, G. 2020, arXiv: [2011.14923](#)
- Hermans, J., Begy, V., & Louppe, G. 2019, arXiv: [1903.04057](#)
- Hermans, J., Delaunoy, A., Rozet, F., Wehenkel, A., & Louppe, G. 2021, *Averting A Crisis In Simulation-Based Inference*, arXiv: [2110.06581](#)
- Hezaveh, Y. D., et al. 2016, *Astrophys. J.*, 823, 37, arXiv: [1601.01388](#), doi: [10.3847/0004-637X/823/1/37](#)
- Hunter, J. D. 2007, *Computing In Science & Engineering*, 9, 90
- Hütten, M., Combet, C., Maier, G., & Maurin, D. 2016, *JCAP*, 09, 047, arXiv: [1606.04898](#), doi: [10.1088/1475-7516/2016/09/047](#)
- Jarvis, M. J., Bacon, D., Blake, C., et al. 2015, arXiv: [1501.03825](#)
- Kerr, F. J., & Lynden-Bell, D. 1986, *Mon. Not. Roy. Astron. Soc.*, 221, 1023
- Kingma, D. P., & Ba, J. 2017, *Adam: A Method for Stochastic Optimization*, arXiv: [1412.6980](#)
- Kluyver, T., et al. 2016, in *ELPUB*
- Lin, M., Chen, Q., & Yan, S. 2014, *Network In Network*, arXiv: [1312.4400](#)
- Lindgren, L., et al. 2018, *Astron. Astrophys.*, 616, A2, arXiv: [1804.09366](#), doi: [10.1051/0004-6361/201832727](#)
- Lisanti, M. 2017, in *Theoretical Advanced Study Institute in Elementary Particle Physics: New Frontiers in Fields and Strings*, 399–446
- McEwen, J. D., Wallis, C. G. R., & Mavor-Parker, A. N. 2021, arXiv: [2102.02828](#)
- Mishra-Sharma, S., Van Tilburg, K., & Weiner, N. 2020, *Phys. Rev. D*, 102, 023026, arXiv: [2003.02264](#), doi: [10.1103/PhysRevD.102.023026](#)
- Mohamed, S., & Lakshminarayanan, B. 2017, *Learning in Implicit Generative Models*, arXiv: [1610.03483](#)
- Mondino, C., Taki, A.-M., Van Tilburg, K., & Weiner, N. 2020, *Phys. Rev. Lett.*, 125, 111101, arXiv: [2002.01938](#), doi: [10.1103/PhysRevLett.125.111101](#)
- Navarro, J. F., Frenk, C. S., & White, S. D. M. 1996, *Astrophys. J.*, 462, 563, arXiv: [astro-ph/9508025](#), doi: [10.1086/177173](#)
- Pardo, K., & Doré, O. 2021, arXiv: [2108.10886](#)
- Paszke, A., et al. 2019, in *Advances in Neural Information Processing Systems 32*, ed. H. Wallach, H. Larochelle, A. Beygelzimer, F. d'Alché-Buc, E. Fox, & R. Garnett (Curran Associates, Inc.), 8024–8035
- Pérez, F., & Granger, B. E. 2007, *Computing in Science and Engineering*, 9, 21, doi: [10.1109/MCSE.2007.53](#)
- Perraudin, N., Defferrard, M., Kacprzak, T., & Sgier, R. 2019, *Astronomy and Computing*, 27, 130, arXiv: [1810.12186](#), doi: [10.1016/j.ascom.2019.03.004](#)
- Piffl, T., et al. 2014, *Astron. Astrophys.*, 562, A91, arXiv: [1309.4293](#), doi: [10.1051/0004-6361/201322531](#)
- Price-Whelan, A., et al. 2018, *Astron. J.*, 156, 123, arXiv: [1801.02634](#), doi: [10.3847/1538-3881/aabc4f](#)
- Read, J. I., Iorio, G., Agertz, O., & Fraternali, F. 2017, *Mon. Not. Roy. Astron. Soc.*, 467, 2019, arXiv: [1607.03127](#), doi: [10.1093/mnras/stx147](#)
- Robitaille, T. P., et al. 2013, *Astron. Astrophys.*, 558, A33, arXiv: [1307.6212](#), doi: [10.1051/0004-6361/201322068](#)
- Sánchez-Conde, M. A., & Prada, F. 2014, *Mon. Not. Roy. Astron. Soc.*, 442, 2271, arXiv: [1312.1729](#), doi: [10.1093/mnras/stu1014](#)
- Saydjari, A. K., & Finkbeiner, D. P. 2021, arXiv: [2104.11244](#)
- Schönrich, R., Binney, J., & Dehnen, W. 2010, *Mon. Not. Roy. Astron. Soc.*, 403, 1829, arXiv: [0912.3693](#), doi: [10.1111/j.1365-2966.2010.16253.x](#)
- Schutz, K. 2020, *Phys. Rev. D*, 101, 123026, arXiv: [2001.05503](#), doi: [10.1103/PhysRevD.101.123026](#)
- Springel, V., Wang, J., Vogelsberger, M., et al. 2008, *Mon. Not. Roy. Astron. Soc.*, 391, 1685, arXiv: [0809.0898](#), doi: [10.1111/j.1365-2966.2008.14066.x](#)
- Stoye, M., Brehmer, J., Louppe, G., Pavez, J., & Cranmer, K. 2018, arXiv: [1808.00973](#)

- 681 Tegmark, M. 1997, Phys. Rev. D, 55, 5895,  
682 arXiv: [astro-ph/9611174](#), doi: [10.1103/PhysRevD.55.5895](#)
- 683 Tejero-Cantero, A., et al. 2020, Journal of Open Source  
684 Software, 5, 2505, doi: [10.21105/joss.02505](#)
- 685 Valogiannis, G., & Dvorkin, C. 2021, arXiv: [2108.07821](#)
- 686 Van Tilburg, K., Taki, A.-M., & Weiner, N. 2018, JCAP,  
687 07, 041, arXiv: [1804.01991](#),  
688 doi: [10.1088/1475-7516/2018/07/041](#)
- 689 Vattis, K., Toomey, M. W., & Koushiappas, S. M. 2020,  
690 arXiv: [2008.11577](#)
- 691 Vegetti, S., Koopmans, L. V. E., Bolton, A., Treu, T., &  
692 Gavazzi, R. 2010, Mon. Not. Roy. Astron. Soc., 408, 1969,  
693 arXiv: [0910.0760](#), doi: [10.1111/j.1365-2966.2010.16865.x](#)
- 694 Vegetti, S., Lagattuta, D. J., McKean, J. P., et al. 2012,  
695 Nature, 481, 341, arXiv: [1201.3643](#),  
696 doi: [10.1038/nature10669](#)
- 697 Virtanen, P., et al. 2020, Nature Methods, 17, 261,  
698 doi: [10.1038/s41592-019-0686-2](#)
- 699 Waskom, M., et al. 2017, mwaskom/seaborn: v0.8.1  
700 (September 2017), v0.8.1, Zenodo,  
701 doi: [10.5281/zenodo.883859](#).  
702 <https://doi.org/10.5281/zenodo.883859>
- 703 WFIRST Astrometry Working Group. 2019, Journal of  
704 Astronomical Telescopes, Instruments, and Systems, 5,  
705 044005, arXiv: [1712.05420](#),  
706 doi: [10.1117/1.JATIS.5.4.044005](#)
- 707 Wilks, S. S. 1938, The Annals of Mathematical Statistics,  
708 9, 60 , doi: [10.1214/aoms/1177732360](#)
- 709 Zonca, A., Singer, L., Lenz, D., et al. 2019, Journal of Open  
710 Source Software, 4, 1298, doi: [10.21105/joss.01298](#)